Flexible optical materials by molecular engineering and integration of perovskite quantum dots and thermoplastic elastomers

A Thesis

Presented to

The Graduate Faculty of The University of Akron

In Partial Fulfillment

of the Requirements for the Degree

Master of Polymer Engineering

Cheng-Han Tsai

March 2023

Flexible optical materials by molecular engineering and integration of perovskite quantum dots and thermoplastic elastomers

Cheng-Han Tsai

Thesis

Approved:

Advisor
Dr. Weinan Xu

Committee Member
Dr. Kevin A. Cavicchi

Committee Member
Dr. Fardin Tayebeh Khabaz

Accepted:

Interim Director of SPSPE
Dr. Mark Soucek

Dean of College
Dr. Craig Menzemer

Interim Director of Graduate School
Dr. Marnie Saunders

ABSTRACT

Metal halide perovskite quantum dots (MHP QDs) are utilized in various applications like solar cell and light-emitting devices due to their unique optoelectronic properties. However, perovskites and their nanomaterials suffer from poor stability due to their susceptibility to moisture, solvent, oxygen, and heat. The absence of effective methods for nanopatterning also hinders their further development and application. To address these issues, we proposed a strategy that involves designed zwitterion polymer ligands synthesis and using them to replace the original small molecule ligands on MHP QDs. Such polymer ligands are expected to improve the stability of those QDs. More importantly, they will enable selective and strong interactions between the MHP QDs and block copolymer thermoplastic elastomers (TPEs) so that soft and stretchable optical materials can be obtained by integrating them. The MHP QDs we focused on are CsPbBr3 QDs, and the block copolymer TPE is poly(styrene-*b*-polyisobutylene-*b*-styrene) (SIBS).

We found that the incorporation of polymer ligands functionalized QDs (p-QDs) into block copolymer TPE leads to changes in the microphase-separated morphology of the TPE matrix, which strongly depends on the molar ratio of p-QDs to copolymer matrix. A relatively high content of QDs (molar ratio of QDs to polymer close to 1) can disrupt the microphase-separated morphology. Moreover, we found that the selective and strong affinity of p-QDs to the TPE matrix leads to higher optical stability of the composites including stronger and longer photoluminescence. Our findings demonstrate the potential of integrating inorganic optical nanomaterials and block copolymer matrix for creating stretchable, soft, and stable optical materials.

TABLE OF CONTENTS

LIST OF FIGURES

CHAPTER I. INTRODUCTION

1.1 Introduction of perovskite quantum dots (QDs)

Perovskites, or more specifically, metal halide perovskites (MHPs), are a class of semiconducting materials with unique optical and electronic properties.[1–4] MHPs have the general chemical composition of ABX_3 (Figure 1a), where A = organic or inorganic cation (such as methylammonium MA^+, Cs^+), B = metal cation (Pb^{2+}, Sn^{2+}, or Bi^{2+}), and X = halide (Cl^-, Br^-, I^-).[5,6] They have been at the forefront of next-generation photovoltaics and optoelectronics due to their efficient optical absorption and emission in the visible range (Figure 1b), the emission of perovskite QDs can be easily tuned by changing the halide composition.[7–9] Besides being used in macroscopic or bulk states, colloidal perovskite QDs can also be synthesized by several methods, which show a strong quantum confinement effect and high external quantum efficiency.[10–12]

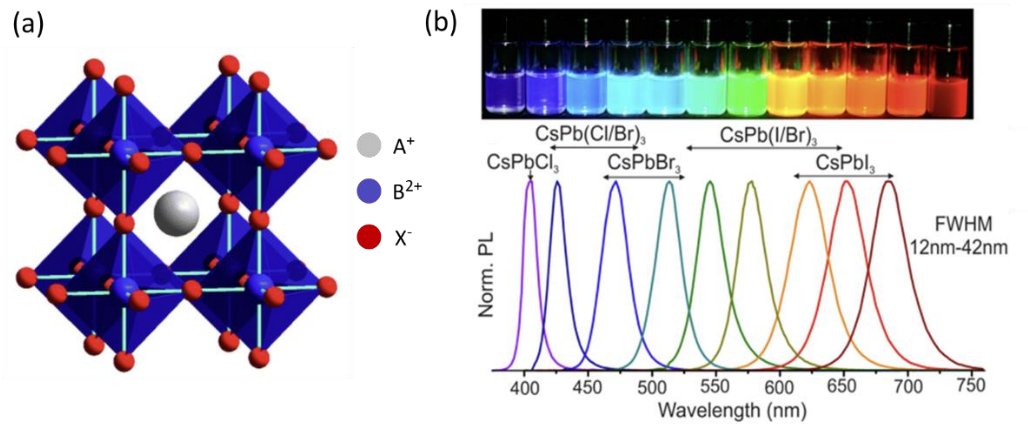

Figure 1. (a) The three-dimensional cubic ABX3 perovskite structure.[13] (b) colloidal solutions in toluene under a UV lamp (λ = 365 nm) and representative PL spectra (λexc = 400 nm for all but 350 nm for CsPbCl3 samples).[7]

However, one of the biggest issues for perovskites and their nanomaterials is poor stability. They are vulnerable to many environmental factors, including moisture, certain solvents, oxygen, and heat.[14–17] MHP QDs with high surface areas are more susceptible to the effects of the environment. Several approaches are being explored to overcome this stability issue, including chemical methods such as capping agents, stabilizers, and physical methods such as device encapsulation;[18–20] but those methods have only limited improvement or require complicated chemical modifications.

On the other hand, the lack of efficient nanopatterning methods for perovskites is another major challenge that prevents their further development and applications.[21] Directly patterning solid perovskite materials with photolithography-based techniques is not feasible due to the poor stability of perovskite under moisture, solvents, and dry etching.[22] Other nanopatterning techniques such as direct laser writing and FIB milling have been used for the nanopatterning of MHP QDs.[23,24] However, those methods are time-consuming, difficult to scale up, and costly. The high-energy beams cause severe structural damage to the MHP QDs and lead to the degradation of photophysical properties.

1.2 Introduction of block copolymer thermoplastic elastomers

Block copolymers (BCPs) are composed of different types of polymers connected at one end. The microphase separation behavior observed in BCP is driven by the chemical incompatibility between the two constituent polymers,[25] resulting in a vast range of morphologies with unique properties. The nature of these morphologies is predominantly determined by intrinsic polymer parameters such as the BCP architecture, interaction parameter (χ), degree of polymerization (N), and volume fraction.[26] The diverse morphologies that arise from BCPs are primarily driven by the thermodynamic mismatch between monomers (χN) and the volume fraction of the blocks (f). These morphologies can range from disordered to ordered structures and can evolve from spherical to lamellar structures during order-order transitions, as depicted in Figure 2. At certain volume fractions, these copolymers can spontaneously organize into well-defined and ordered nanoscale patterns such as spheres, cylinders, or lamellae.[27–30] The size of these domains is influenced by the molecular weight of the copolymer and the strength of the interactions between the different types of blocks. The domain size of the microphase-separated structure in BCP is typically in the range of several to tens of nanometers (nm), which is in the same range as many inorganic nanoparticles (NPs). The hybrid materials based on the co-assembly of BCP, and metal NPs have tunable and organized nanostructures.[31,32] The morphology, domain size, and properties of polymers forming each segment, such as solubility, surface energy, refractive index, mechanical strength, and glass transition temperature, offer a vast range of potential applications for phase-separated copolymers. These copolymers have already found usage in various fields, including adhesives, dispersants, surfactants, and thermoplastic elastomers. Photonic crystal devices, membranes, and more.[33]

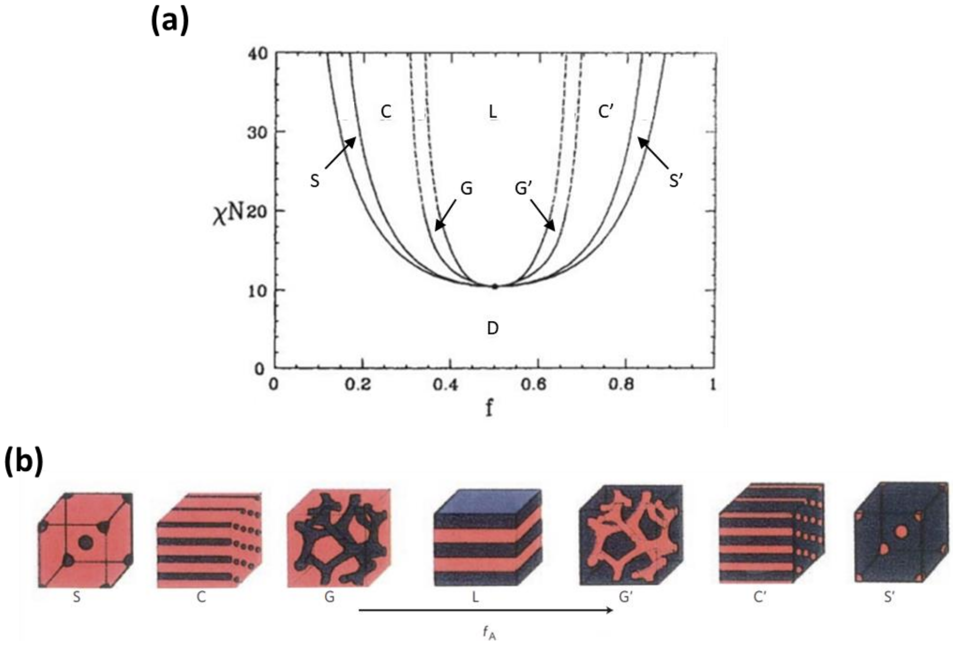

Figure 2. (a) Phase diagram depicting the behavior of liner BCP (A-*b*-B) is determined by the interaction parameter (χN)and the volume fraction (*f*). Four equilibrium

morphologies, namely spherical (S), cylindrical (C), gyroid (G), and lamellar (L).[34] (b) Phase structures are depicted with the volume fraction (f_A) of one of the components being the independent variable at a constant χN value. The red and black components are used to represent the different constituents of the copolymer.[33]

Nanocomposites are materials composed of one or more components that have nanostructure, consisting of hierarchically-structured nanoparticles that are made up of single particles. To create specific functional nanocomposites, it is important to choose appropriate NPs as the building blocks. Additionally, these approaches must be adapted for NPs with varying chemical compositions, sizes, and shapes.[35–38] The NPs are typically localized in the microdomains of one of the blocks or at the interface between the microdomains.[35–46] This approach has been extensively studied for the past several decades for precise assembly and nanopatterning of various inorganic NPs, including metals,[51–53] semiconductors [54,55], and dielectrics.[56–58] With the discovery of new types of functional inorganic NPs, especially perovskite nanomaterials, their molecular interactions and controlled assembly with BCPs have the potential to generate new types of optical materials that are soft, stretchable, highly stable, and nano-patternable. [59–63]

A type of polyisobutylene (PIB) based block copolymer, poly(styrene-*b*-isobutylene-*b*-styrene) (SIBS), where PIB is an elastomeric segment, and polystyrene (PS) is a rigid segment.[64] Chemical structure of SIBS is shown in Figure 3. The domain size of microphase separated structure in BCP is typically in the range of several to tens of nanometers (nm).[65–68] It has excellent chemical, oxidative, and biostability[69–71], extremely low permeability, as well as high strength and elongation at break (> 600%).[72] Those advantages make it a perfect soft material to be assembled with NPs to create soft, stretchable, stable hybrid materials with molecular-level control of the interfacial and internal structure.

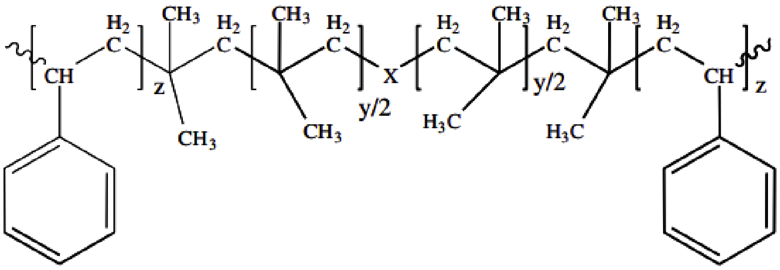

Figure 3. Chemical structure of SIBS[69]

CHAPTER II. OBJECTIVE AND HYPOTHESIS

2.1 Research Objective

This project aims to fill this knowledge gap by systematically investigating and elucidating the molecular interactions and controlled assembly of chemically functionalized MHP QDs and BCP. Moreover, we designed and customized the surface chemistry of the MHP QDs and the ionic state of the polymer blocks in styrenic TPEs, which enabled high compatibility and highly selective interaction and alignment between the rigid MHP QDs and soft microphase separated matrices. SIBS's advantages make it a perfect soft material to be assembled with MHP QDs to create soft, stretchable, stable hybrid materials with molecular-level control of the interfacial and internal structure.

In this study, we designed and conducted a ligand exchange reaction to replace short ligands (oleic acid and oleylamine) on MHP QDs with chemically modified poly(isobutylene-*g*-maleic anhydride) (PIMA), which had strong and selective interaction with the PIB block in SIBS copolymer due to their matching chemical composition and interaction parameters. The solution mixing approach will be employed to integrate the

MHP QDs with SIBS by adjusting the ratios of two components to achieve different hybrid nanostructures.

2.2 Hypothesis

- By attaching designed polymer ligands to MHP QDs and/or tuning the ionic state of the PS block in the TPE matrix, we anticipate achieving precise assembly and alignment of MHP QDs in the TPE matrix. This will provide unprecedented freedom in the design of hybrid optical materials.
- By matching the surface chemistry of multiple different types of MHP QDs with the polymer blocks in the TPE matrix, we anticipate achieving simultaneous assembly and alignment of two or more different types of MHP QDs in a microphase-separated soft matrix.
- By incorporating perovskite materials into the TPE matrix, especially the PIB-based TPE, we expect to observe superior chemical stability, impermeability to gases/vapors, biostability, and excellent mechanical properties in the resulting hybrid materials. This is expected to substantially enhance the stability and introduce new applications for perovskite materials that were previously unattainable.

CHAPTER III. MATERIALS AND METHODS

3.1 Materials

Highly Reactive Polyisobutylene (Glissopal V1500 HR-PIB, BASF, Mn 2300), benzoyl peroxide (BPO, ≥ 98%, Sigma Aldrich), chloroform (Approx. 0.75% Ethanol as Preservative, Fisher Chemical), acetone (Certified ACS, Fisher Chemical), 3-Dimethylaminoproplyamine (99%, Thermo Scientific), 1,4-dioxane (ACS reagent, ≥99%, Sigma Aldrich), di-tert-butyl decarbonate ($(Boc)_2O$, 95.0+%, TCI), ethyl acetate (Fisher Chemical), sodium sulfate (99%, Thermo Scientific), N,N-Dimethylformamide (DMF, ≥ 99.8%, Sigma Aldrich), 1,3-propanesultone (99%, Thermo Scientific), diethyl ether (Fisher Chemical), methylene chloride (Fisher Chemical), 4M hydrogen chloride in 1,4-dioxane (99%, Fisher Chemicals), triethylamine (99%, Thermo Scientific), methanol (certified ACS, Sigma Aldrich), toluene (Certified ACS, Fisher Chemical), toluene anhydrous (99.8%, thermos scientific), tetrahydrofuran (THF, HPLC grade, > 99.9%, Sigma Aldrich), poly(styrene-*b*-isobutylene-*b*-styrene) (SIBS 073T, $M_n = 66{,}720$ g/mol, 31 wt% PS, and SIBS 062T, $M_n = 60{,}000$ g/mol, 23 wt% PS, KENEKA Corporation), maleic anhydride (MA, 99%, Thermo Scientific) was dried under vacuum at room temperature for 2 h in vacuum oven before using. $CsPbBr_3$ perovskite nanoparticles were provided by Dr. Yitong Dong's lab at The University of Oklahoma.

3.2 PIMA synthesis through the solvothermal method

The reaction condition was adopted from a previous study.[73] To synthesize the maleic anhydride graft onto highly reactive polyisobutylene (HR-PIB), free radical polymerization and solvothermal method were induced (Figure 4). The schematic illustration of free radical graft copolymerization of maleic anhydride (MA) onto HR-PIB. 0.136 g (0.56 mmol) BPO, 1.950 g (20 mmol) MA, 15.63 g (6.8 mmol) HR-PIB, and 15 mL chloroform were sealed into an autoclave. The vessel was heated to 110˚C under vacuum for 3 h and cooled to room temperature. The transparent viscous product was washed with acetone by centrifugation at 4000 rpm for 10 min at least three times to remove the excess MA. The purified product was dried under vacuum at 60˚C overnight. The final product was a transparent viscous liquid.

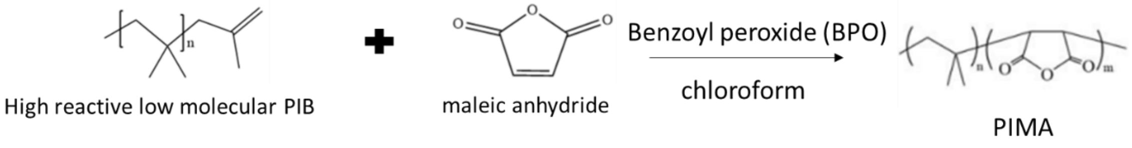

Figure 4. schematic illustration of free radical graft copolymerization of MA onto highly reactive PIB (HR-PIB)

3.3 Amine-modified sulfobetaine zwitterion synthesis

All the chemicals involved with amine-modified sulfobetaine zwitterion (NH_2-ZW) synthesis and $CsPbBr_3$ QDs solution were handled in the glove box, and all the chemical reactions were taken placed in the fume hood and connected to the Schlenk line.

The reaction condition and steps were adopted from previous studies with few modifications.[74,75] The schematic of the chemical reaction of NH_2-ZW synthesis was shown in Figure 5. In this study, the reaction was split into three reaction steps. First, we used N-Boc-dimethylaminopropylamine (Boc), a protection reagent, to protect the primary amine group of N, N-dimethylaminopropylamine. Secondly, 1,3-propane sultone coupled to the tertiary amine at the end of the intermediate. Last, an excess strong acid (HCl) was used to eliminate the Boc group and free the primary amine to form NH_2-ZW.

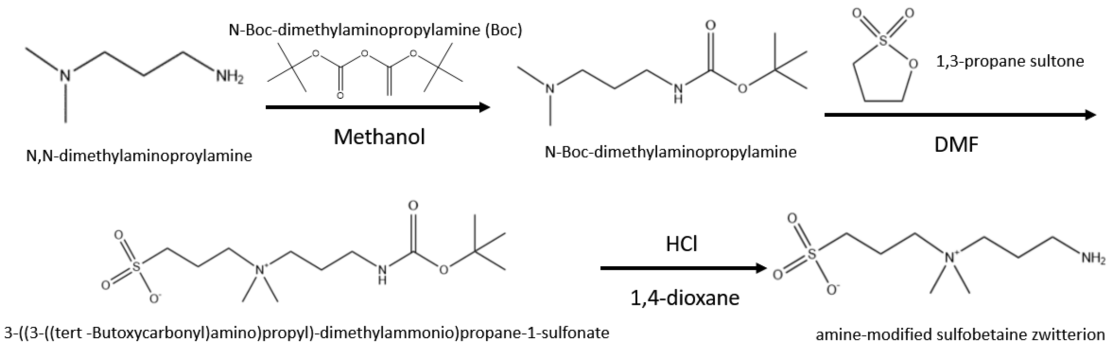

Figure 5. Scheme of chemical reaction of overall NH2-ZW synthesis

Figure 6 shows the scheme of reaction for step I. 2 mL (0.016 mol) of N, N-dimethylaminoproylamine was dissolved in 17 mL 1,4-dioxane, then 5.47 mL (0.024 mol) of Di-tert-butyl decarbonate (Boc) was added dropwise to the mixed solution at 0°C with stirring for 2 h and purged with N_2. The mixed solution was then warmed up to room temperature and kept stirring for one day. The solvent, 1,4-dioxane, was evaporated by a rotary evaporator. The compound was dissolved in 50 mL of DI water and was extracted by ethyl acetate. It was extracted at least three times. The water phase was discarded, and the ethyl acetate phase was collected in a 100 mL conical flask. Sodium sulfate was added to the solution to remove water from the solution. The solvent, ethyl acetate, was evaporated by a rotary evaporator. 1.825 g (9 mmol) of the yellowish oil-like product (Figure 9a) was obtained.

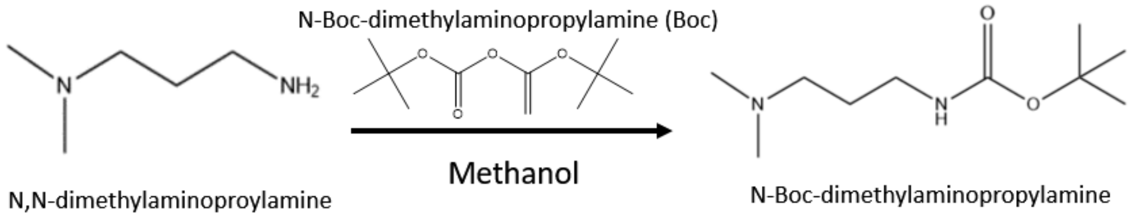

Figure 6. Scheme of Step I reaction

The scheme of the step II reaction is shown in Figure 7. 1.825 g (9 mmol) of the compound obtained from step I was dissolved in 7.5 mL DMF, then 1.17 mL (13.3 mmol) of 1,3-propane sultone was added to the mixed solution. The solution was stirred at room temperature for two days and purged N_2. The solvent, DMF, was evaporated by using a rotary evaporator. The yellow sticky compound was dispersed with 15 mL of diethyl ether and stirred for 10 min. The diethyl ether with residual 1,3 propane sultone was decanted. The product was dried under vacuum in a vacuum oven at room temperature. 4.13 g (12.7 mol) yellow paste product (Figure 9b) was obtained.

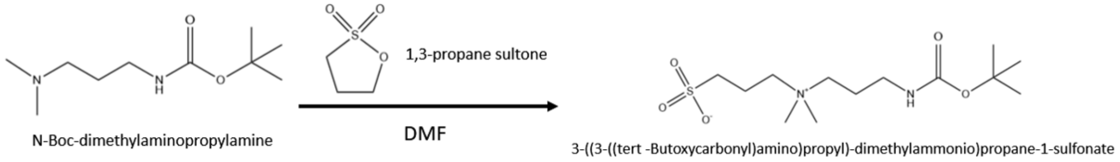

Figure 7. Scheme of Step II reaction

The scheme of the step III reaction is shown in Figure 8. 2.86 g (9 mmol) of the compound obtained from step II was dissolved in 60 mL of methylene chloride in a round bottom flask with stirring at 0˚C, then 6 mL of 4M HCl in 1,4-dioxane was added dropwise into the mixed solution, and stirred for 30 min. The white viscous solid was precipitated after stirring for 30 min (Figure 9c). The solution was discarded, then 2.5 mL of triethylamine was added to the glass vial to remove residual HCl. White solid salt was formed then 3 mL of chloroform was added to the glass vial to dissolve to remove the salt. The supernatant was discarded. The viscous product was recrystallized in methylene chloride/methanol. The product was collected and dried at 40 ˚C in a vacuum oven overnight. 1.5473 g of NH_2-ZW was obtained (Figure 9d). The product yield is 56.7%.

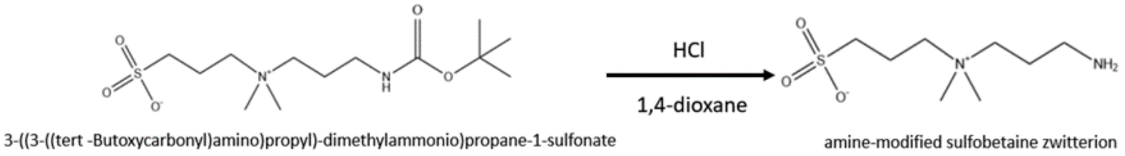

Figure 8. Scheme of Step III reaction

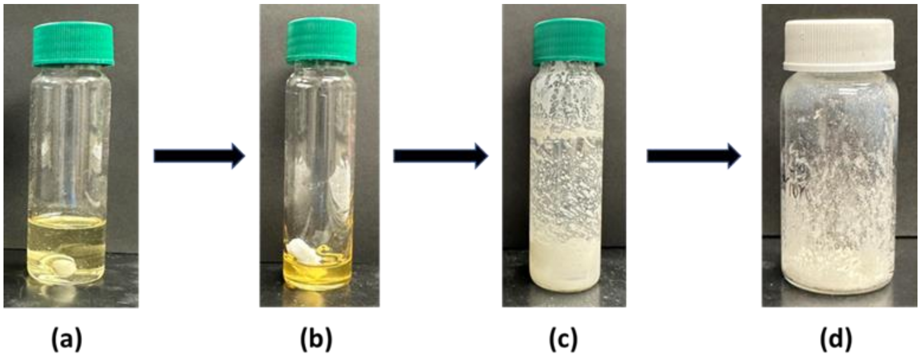

Figure 9. Product images and representative process of the NH2-ZW synthesis. (a) Yellowish oil-like product after the Boc reaction. (b) Yellow paste product after reacting with 1,3 propane sultone. (c) Addition of 4M HCl and stir for 30 min. (d) White solid After recrystallizing and drying in a vacuum oven

3.4 Chemically modified PIMA synthesis

The chemical reaction condition and steps were studied from the previous study[73] with few modifications. The scheme of the ring-opening reaction for PIMA is shown in Figure 10. 2 g (0.46 mmol) PIMA polymer was dissolved in 10 mL of toluene in the round bottom flask. 0.746 g (3.33 mmol) of NH_2-ZW was dissolved in 17 mL of methanol. The

17 mL of NH_2-ZW solution was added dropwise into the polymer solution while stirring and was stirred at 55˚C overnight. The white viscous product was precipitated at the bottom of the flask. The supernatant was decanted, then 10 mL of toluene was added to the round bottom flask to dissolve the product. The ligand solution was added dropwise into 400 mL of methanol under vigorous stirring. The polymer ligand was precipitated at the bottom of the beaker. The white viscous polymer ligand was collected into a 40 mL glass vial and was dried under vacuum at 40˚C overnight. 1.5032 g white viscous polymer ligand was obtained.

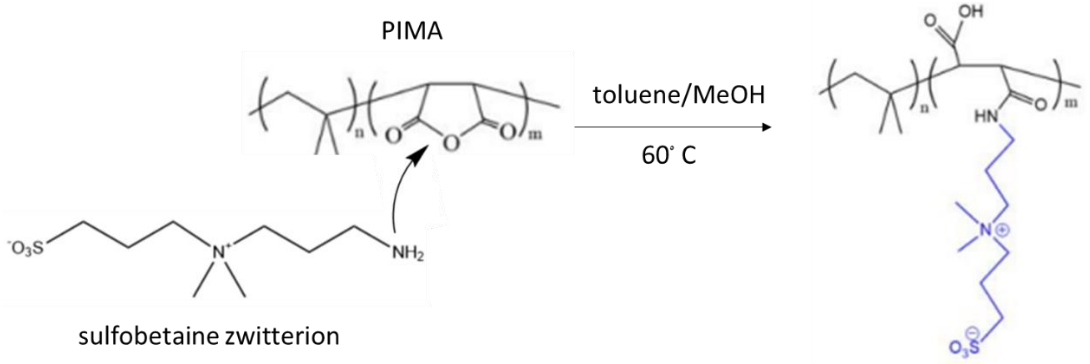

Figure 10. Scheme of the ring-opening reaction for PIMA

3.4 $CsPbBr_3$ QDs synthesis

A precursor of Cs-oleate was made by dissolving of Cs_2CO_3 in a mixture of oleic acid (OA) and 1-octadecene (ODE) at 150 ˚C. The temperature of the Cs-oleate solution was kept above 100 ˚C. To make a precursor solution for Pb and Br, $PbBr_2$ and $ZnBr_2$ were dissolved in a mixture of ODE, OA, and oleylamine (OLA) at 120 ˚C. Cs precursor solution was added to the precursor solution of Pb and Br to initiate the reaction. Once the reaction was cooled down, the $CsPbBr_3$ QDs were purified with several purification steps. Further information regarding the $CsPbBr_3$ QDs synthesis can be found in previous studies.[3,4]

3.5 $CsPbBr_3$ QDs ligand exchange

0.03026 g ($7x10^{-6}$ mol) chemically modified PIMA ligand was dissolved in 1.5 mL anhydrous toluene. The chemically modified PIMA was filtered with a syringe filter before mixing with $CsPbBr_3$ QDs solution. 70 μL of $CsPbBr_3$ QDs solution and 1.5 mL of polymeric ligand solution were mixed in a glass vial. The solution was stirred at room temperature for 10 min. The image shows the mixed solution after the ligand exchange process.

3.6 $CsPbBr_3$ QDs and SIBS composites preparation

A hybrid solution was prepared by dissolving 073T and 062T SIBS in toluene and mixing it with a solution of polymer ligands exchanged $CsPbBr_3$ QDs (p-QDs). The molar ratio of SIBS to p-QDs in the 073T and 062T SIBS samples were 1 : 1 and 5 : 2, respectively. The mixing solution was spin-coated onto a cover glass to form a thin film at 6000 rpm for 30 s.

3.7 Characterization

3.7.1 Nuclear Magnetic Resonance (NMR) Spectrometer

Mercury-300 NMR was used to characterize the structure of NH_2-ZW and the structure of the compounds from each step of NH_2-ZW synthesis. Before testing, the compounds were dissolved in D_2O or $CDCl_3$.

3.7.2 Fourier-transform infrared spectrometer (FTIR)

Nicolet iS50 FTIR spectrometer was used to confirm the structure of PIMA and chemically modified PIMA by using Attenuated Total Reflection (ATR) mode.

3.7.3 UV-Vis Spectroscopy

Agilent 8453 UV-Vis spectroscopy was used to understand the optical properties of the perovskite QDs solution. The QDs and p-QDs solution samples were prepared with the same mole of QDs and diluted by adding the same volume of toluene.

3.7.4 Photoluminescence (PL) spectrophotometer

Cary Eclipse PL spectrophotometer was used to characterize the optical properties of the perovskite QDs solution, p-QDs solution, and SIBS/p-QDs hybrid films. The solution samples were prepared with the same mole of QDs and diluted by the same amount of toluene. The hybrid films were fabricated with the same mole of QDs and spin-coated with the same rate and time.

3.7.5 Atomic Force Microscopy (AFM)

Bruker Dimension Icon AFM was used to figure out the morphology of the p-QDs/SIBS hybrid film. AFM images were obtained in tapping mode, where the resonance frequency was adjusted to 270 kHz and the scan rate was set as 0.8 Hz. The AFM images were modified by using Gwyddion software.

CHAPTER IV. RESULT AND DISCUSSION

This chapter provides an overview of the reaction steps involved in the design of polymeric ligands, which we successfully synthesized and characterized by NMR and FTIR. control experiments were conducted to compare the stability of the perovskite QDs before and after p-QDs. Moreover, we investigated whether blending SIBS with perovskite QDs with polymeric ligands could enhance the stability of the QDs. Furthermore, we analyzed the morphology of the SIBS/p-QDs hybrid films, providing valuable insights into the compatibility of these materials and their potential applications.

4.1 Synthesis of zwitterionic polymer ligands

4.1.1 Synthesis of PIMA

FTIR was used to compare the spectra of PIMA with that of pure HR-PIB (Figure 11). The comparison reveals the appearance of four new peaks at 1076, 1724, 1780, and 1860 cm^{-1}, which are attributed to the presence of maleic anhydride. Among these peaks, the C=O stretching of the anhydride rings in maleic anhydride is identified at 1860 cm^{-1}, while the peak at 1780 cm^{-1} is assigned to the C=O stretching of the anhydride rings as well.[76] Additionally, the peak at 1076 cm^{-1} corresponds to the stretching of the =C-O-C= group, which is a characteristic peak contributed by maleic anhydride.[77] The presence of the carboxylic acid peak at 1724 cm^{-1}, which is caused by the hydrolysis of the anhydride group, further confirms the presence of maleic anhydride.[78] The C-H stretching vibrations of the methyl groups ($-(CH_2-C(CH_3)_2)_n-$) in the main chain of HR-PIB is detected at 1388 and 1364 cm^{-1}, and their characteristics peak remains strong.[78] Additionally, an absorption peak at 893 cm^{-1} was observed, which was attributed to the out-of-plane deformation of vinyl groups in the HR-PIB chain.[78] These findings indicate that the maleic anhydride has successfully reacted with PIB to form PIMA.

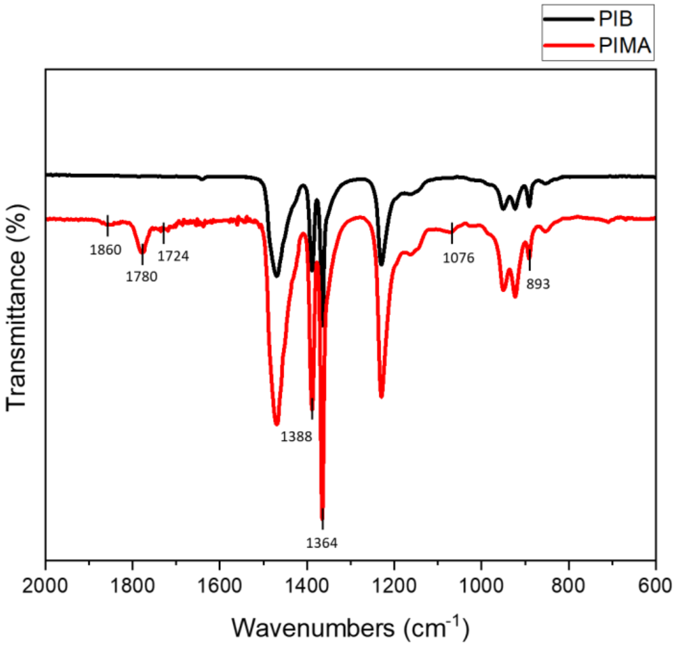

Figure 11. FTIR of HR-PIB and PIMA

The relative degree of grafting (RDG) and degree of grafting (DG) were investigated by the previous study.[73] RDG was calculated based on the intensity ratio of specific IR peaks (Figure 11) by equation (1).[73]

$$\mathrm{RDG} = \frac{I_{1860+1780\ cm^{-1}}}{I_{1388\ cm^{-1}} + I_{1364\ cm^{-1}}} \qquad (1)$$

In equation (1), it's the ratio of intensities of maleic anhydride peaks in 1690-1890 cm^{-1} and 1388 cm^{-1} and 1364 cm^{-1} are the intensities of peaks of highly reactive PIB. The relationship between RDG and DG is concluded by the following equation (2).[73]

$$\mathrm{DG} = 1.76\ \mathrm{RDG} \qquad (2)$$

4.1.2 Synthesis of sulfobetaine zwitterion

The synthesis of sulfobetaine zwitterion involves three reaction steps. In the first step, the starting material N, N-dimethylaminopropylamine, which has a primary amine group and a tertiary amine group, is reacted with tert-butyloxycarbonyl (Boc) through a substitution reaction. Boc is used to protect the primary amine group. In the second step, the yellow oil-like compound resulting from the first reaction is reacted with 1,3-propane sultone through a nucleophilic reaction. Lastly, the yellow paste compound obtained from the second reaction is reacted with strong acid 4M HCl, which protonates the amide group removing the Boc and freeing the amine group.

The ^{1}H NMR spectroscopy analysis was carried out to investigate the chemical structure after the Boc protection (Figure 12). The spectrum displays a new resonance at 1.40 ppm, corresponding to the methyl groups of the Boc, confirming the successful introduction of the Boc protection group. Additionally, a new resonance at 5.17 ppm is observed, which can be attributed to the amide group formed during the reaction. The appearance of these new peaks indicates the successful formation of the desired intermediate chemical structure. ^{1}H NMR (Figure 12), δ (ppm) = 3.14 (m, 2H, -CH$_2$-C***H***$_2$-NH-), 2.27 (t, 2H, -NH-C***H***$_2$-CH$_2$-), 2.17 (s, 6H, -CH$_2$-N-(C***H***$_3$)$_2$) 1.59 (m , 2H, -CH$_2$-C***H***$_2$-CH$_2$-), 1.40 (s, 9H, -C(C***H***$_3$)$_3$).

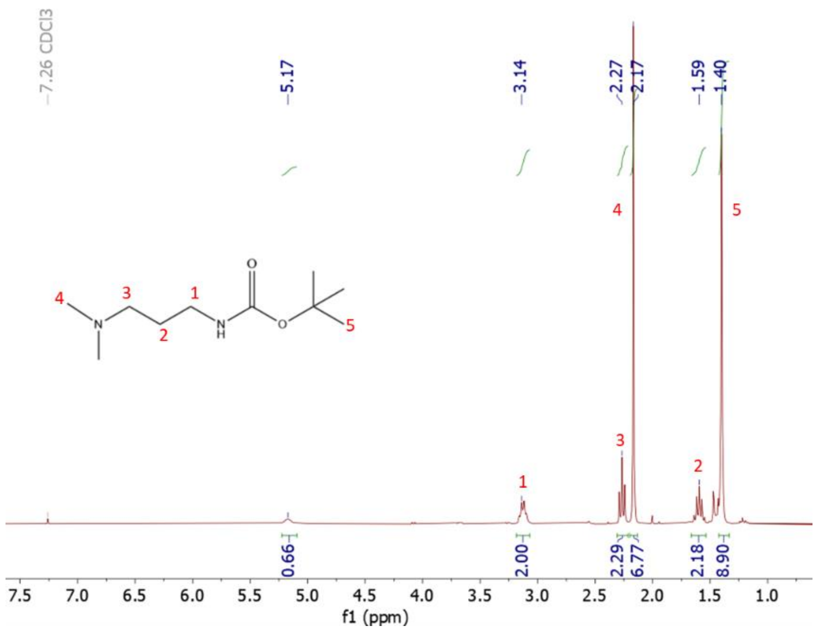

Figure 12. 1H NMR spectrum of Step I (in CDCl$_3$)

The ^{1}H NMR spectrum was used to confirm the chemical structure following the reaction with 1,3 propane sultone, as shown in Figure 13. The appearance of new resonances at 1.80, 3.02, and 3.31 ppm, corresponding to the methylene groups of the 1,3 propane sultone is indicative of the reaction's success. Moreover, the resonance at 3.14 ppm shifts upfield to 2.69 ppm after the reaction. The resonances at 1.59 and 2.27 ppm shift downfield to 2.05 and 3.20 ppm, respectively, upon reacting with 1,3 propane sultone. ^{1}H NMR (Figure 13), δ (ppm) = 3.31 (m, 2H, $-CH_2-C\boldsymbol{H_2}-$ $N(CH_2)_2-$), 3.20 (m, 2H, $-N(CH_2)_2-C\boldsymbol{H_2}-CH_2-$), 3.02 (m, 2H, $-CH_2-C\boldsymbol{H_2}-SO_3$), 2.84 (s, 6H, $-CH_2-N(C\boldsymbol{H_3})_2-CH_2$), 2.69 (t, 2H, $-CH_2-C\boldsymbol{H_2}-NH-$), 2.05 (m, 2H, $-CH_2-C\boldsymbol{H_2}-CH_2-NH-$), 1.80 (m, 2H, $SO_3-CH_2-C\boldsymbol{H_2}-CH_2-$), 1.27 (s, 9H, $-C(C\boldsymbol{H_3})_3$).

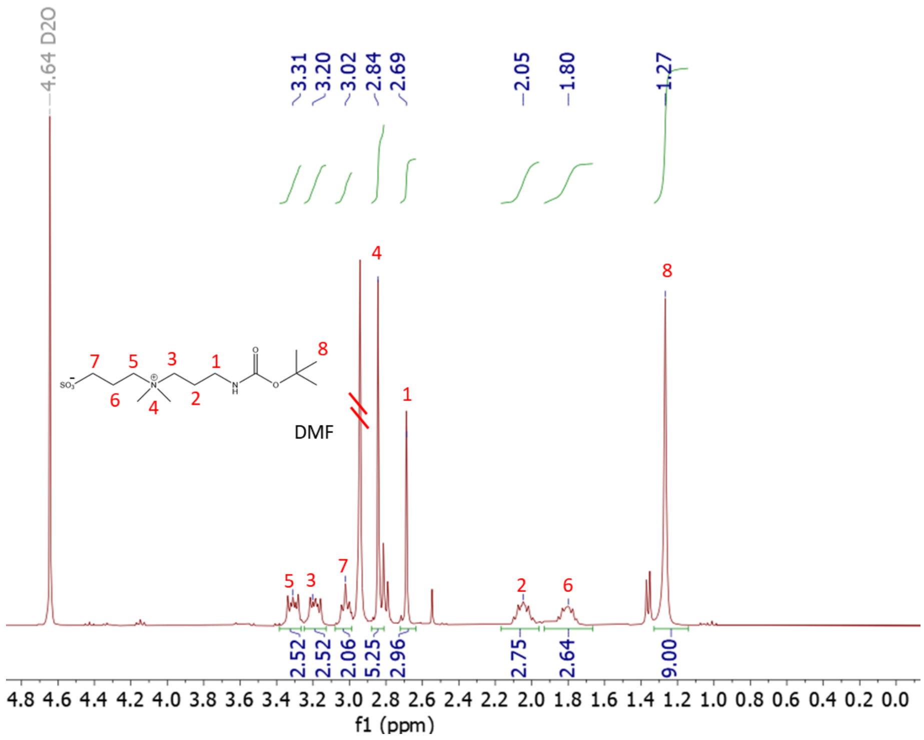

Figure 13. 1H NMR spectrum of Step II (in D2O)

The chemical structure of ZW-NH$_2$ was confirmed by the ^{1}H NMR spectrum (Figure 14). The resonance at 1.27 ppm disappears corresponding to the methyl groups of Boc that were removed by HCl. The ^{1}H NMR spectrum also shows the absence of any residual Boc-protecting group. ^{1}H NMR (Figure 14), δ (ppm) = 3.39 (m, 2H, -CH$_2$-C$\boldsymbol{H_2}$-N(CH$_2$)$_2$-), 3.32 (m, 2H, -N(CH$_2$)$_2$-C$\boldsymbol{H_2}$-CH$_2$-), 3.02 (s, 6H, -CH$_2$-N(C$\boldsymbol{H_3}$)$_2$-CH$_2$), 2.97 (t, 2H, -CH$_2$-C$\boldsymbol{H_2}$-SO$_3$), 2.09 (m, 4H, -CH$_2$-C$\boldsymbol{H_2}$-CH$_2$-N(CH3)$_2$-CH$_2$-C$\boldsymbol{H_2}$-CH$_2$-).

In summary, the ZW-NH_2 was confirmed by ^{1}H NMR spectroscopy, which reveals that the resonance at 1.40 ppm corresponding to the Boc methyl groups appears after the Boc protection reaction (Figure 12) and new resonances corresponding to methylene groups of the 1,3 propane sultone are observed after reacting with 1,3 propane sultone (Figure 13). In the ^{1}H NMR spectrum of ZW-NH_2 (Figure 14), the disappearance of the resonance at 1.27 ppm confirms the removal of Boc methyl groups by HCl.

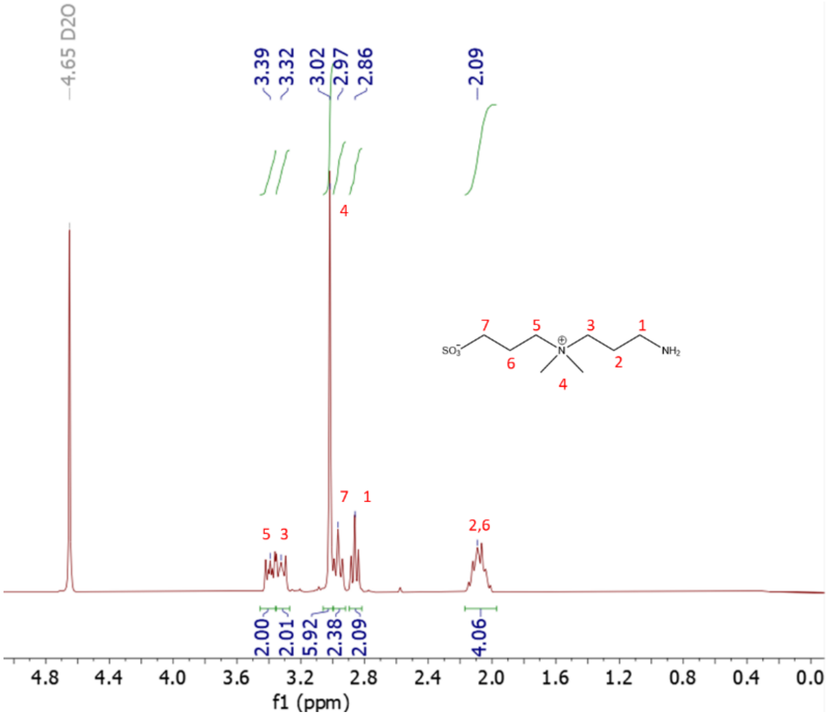

Figure 14. ^{1}H NMR spectrum of ZW-NH_2 (in D_2O)

4.1.3 Synthesis of chemically modified PIMA

The chemically modified PIMA was carried out through a ring-opening reaction. The chemical structure of chemically modified PIMA was confirmed by the FTIR spectrum. By comparing the FTIR spectra of chemically modified PIMA and PIMA shown in Figure 15, it is observed that a new peak emerges at 1073 cm^{-1} after ZW-NH$_2$ reacted with maleic anhydride in PIMA. The board peak at 1073 cm^{-1} contributes to the S=O stretching of the sulfoxide group present in ZW-NH$_2$. After the ring-opening reaction of PIMA, the FTIR spectrum of the resulting chemically modified PIMA shows two peaks at 1388 and 1364 cm^{-1}, which contributes to the C-H stretching vibrations of the methyl groups (-(CH$_2$-C(CH$_3$)$_2$)$_n$-) in the main chain of HR-PIB, which remains unchanged. These results suggest that the chemically modified PIMA was successfully synthesized.

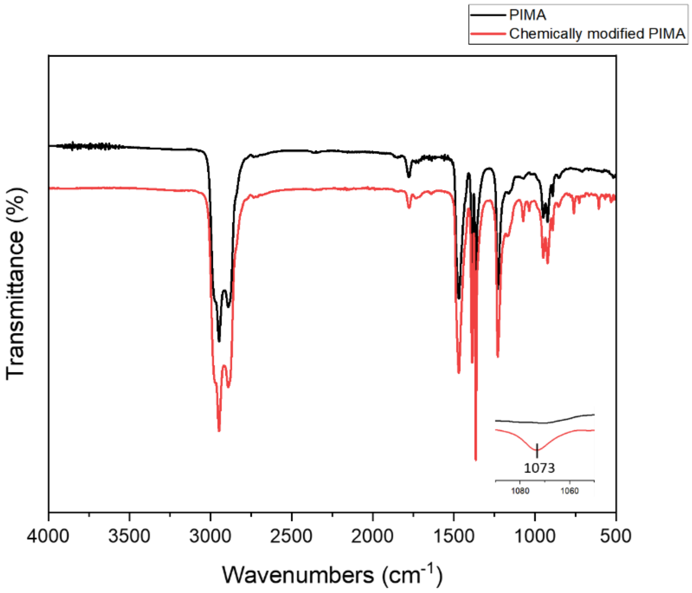

Figure 15. FTIR of PIMA and Chemically modified PIMA

4.2 Polymer Ligands exchange and Optical properties of $CsPbBr_3$ QDs and p-QDs

The optical properties of $CsPbBr_3$ QDs and p-QDs are of great interest in their potential use in various applications, such as in photovoltaics and optoelectronics. Therefore, understanding the mechanisms that affect their stability and optical properties is crucial for their effective utilization. Several factors could influence the stability of QDs, such as moisture, certain solvents, oxygen, and heat. These factors can cause degradation and lead to the formation of defects. Therefore, it is essential to investigate the stability and optical properties of QDs and p-QDs. Additionally, the properties of the ligands used to passivate the surface of the QDs could also affect their stability and optical properties. For instance, some ligands may have a better affinity towards the surface of the QDs, leading to improved passivation and stability, while others may not be as effective.

The optical properties of $CsPbBr_3$ QDs and p-QDs were analyzed through UV-Vis spectroscopy and PL spectroscopy as presented in Figure 16. Interestingly, the results indicate that the exchange of the ligand led to a slight shift in both absorption and emission peaks towards shorter wavelengths. This shift can be attributed to various factors, including surface passivation and ligand-capping effects, which can alter the energy levels and excited state of the QDs. However, the blue shift observed in the spectra of the p-QDs is even more complex and may be due to the photo-oxidation process, which can create free radicals and reactive oxygen species that attack the surface of QDs and the passivation layer of QDs, leading to the formation of surface defects and trap states. This process, along with chemical degradation, can lead to the release of heavy metal ions, instability of the QDs surface, and effective size shrinkage[79–81], ultimately causing a uniform reduction in size and corresponding blue shift observed in the PL spectra of p-QDs can also result from a decrease in absorption cross-section of individual QDs, implying a reduction in their effective size. [82,83]

The degradation of $CsPbBr_3$ QDs upon exposure to oxygen and humidity is a critical challenge to their practical applications since it leads to the formation of surface defects, nonradiative recombination centers, and a decrease in the overall intensity of the QDs. Moreover, the reduction in the size of the semiconducting core of the QDs increases the band gap energy, further contributing to the observed blue shift in their spectra (Figure 17). However, p-QDs have slightly faster degradation rates than $CsPbBr_3$ QDs, the p-QDs still have strong and stable fluorescence emission after seven days, with the emission peak at 475 nm. This indicates that the band gap and crystalline structure of p-QDs were relatively unaffected by the degradation process, and the material still has the potential to be utilized in practical applications that require stable and long-lasting optical properties under ambient conditions. In summary, the stability test results suggest that p-QDs are stable under ambient conditions and retain their strong and stable fluorescence emission.

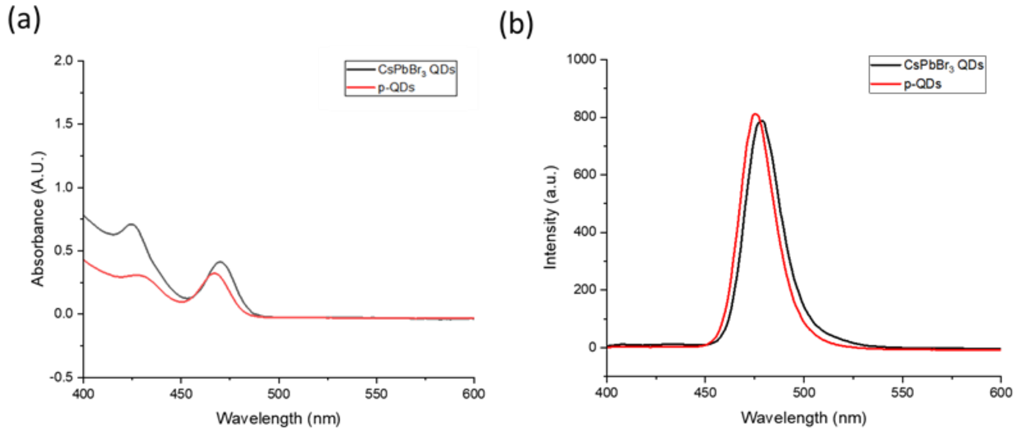

Figure 16. (a) UV-Vis spectra of $CsPbBr_3$ QDs (black line) and $CsPbBr_3$ p-QDs (red line). (b) PL spectra of $CsPbBr_3$ QDs (black line) and $CsPbBr_3$ p-QDs (red line).

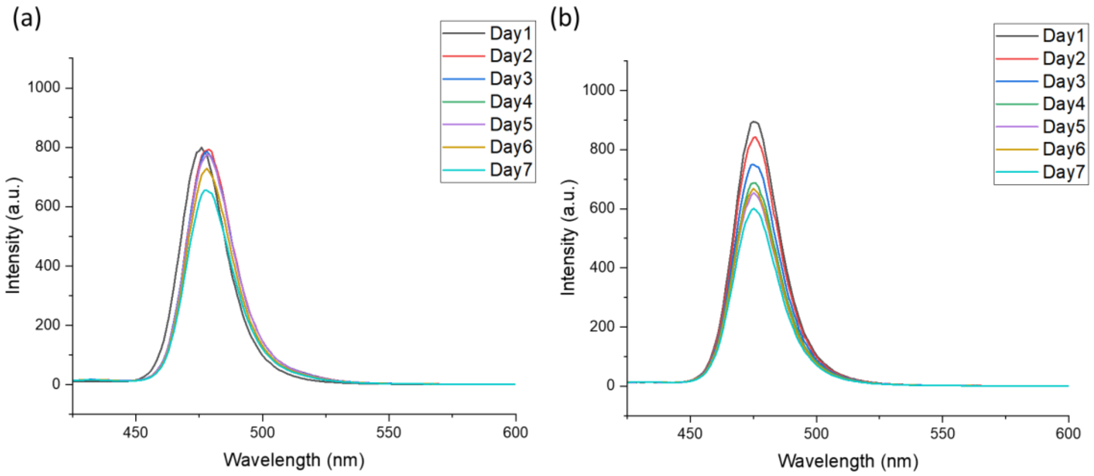

Figure 17. Long-term light emission of (a) $CsPbBr_3$ QDs and (b) $CsPbBr_3$ p-QDs solution

4.3 Composite films of SIBS and CsPbBr3 p-QDs

The optical properties of 073T and 062T SIBS thin films with different molar ratios of p-QDs were characterized using PL spectroscopy (Figures 18 and 19). The hybrid films emit pure and blue light when observed under UV light, which suggests that the incorporation of SIBS did not significantly affect the light emission of the p-QDs. Moreover, the observed light emissions of the hybrid films were consistent with the results obtained from the PL peak measurements, which showed a wavelength of 476nm. These findings demonstrate the compatibility and potential of p-QDs as a versatile luminescent material for the development of hybrid organic-inorganic thin film with optical properties.

we employed the PL spectrum to evaluate the stability of the films. The SIBS/QDs hybrid films, which served as control samples (Figure 18a and 19a), show significant degradation after 7 days, with most of the QDs' crystalline structure being damaged by oxygen and moisture, resulting in a loss of their optical properties. Notably, despite the films exhibiting degradation, degradation is much slower and their optical properties remained unchanged without any peak shifting, indicating that most QDs could maintain their crystalline structure after 7 days. This suggests that the polymer ligands effectively provided QDs with the high affinity of SIBS, which the ability of the polymer to block ambient oxygen from reaching the QDs' surface is the probable reason for the protection of QDs against photoinduced degradation.[79]

Interestingly, an increase in PL intensity is observed for the SIBS/QDs film (Figure 18a) and SIBS/p-QDs film (Figure 19b) on day 5, which may be attributed to photobrightening.[84] This phenomenon is believed to be caused by photoactivation and has been linked to various factors, including the passivation of surface traps.[83] Moisture exposure can have positive effects on the properties of perovskite QDs. It has been found that controlled exposure to a certain level of moisture can decrease the trap density in the materials.[85]

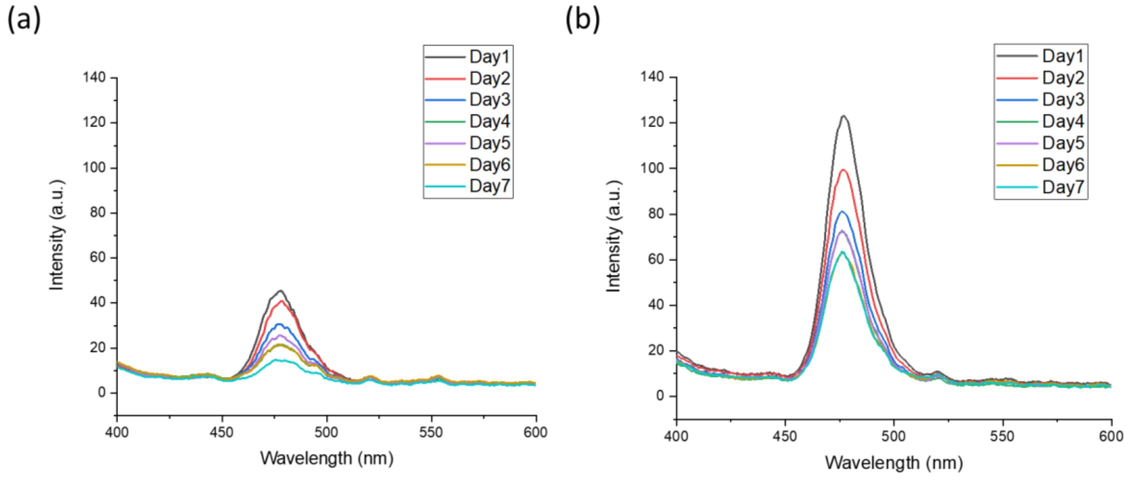

Figure 18. PL spectra of (a) 073T SIBS/CsPbBr3 QDs hybrid film and (b) 073T SIBS/p-QDs hybrid film with a molar ratio of 1 : 1

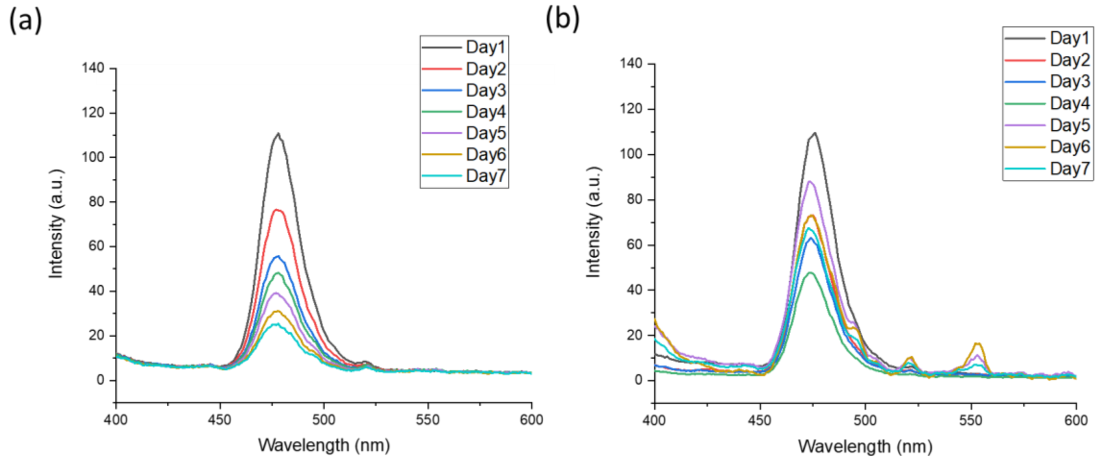

Figure 19. PL spectra of (a) 062T SIBS/CsPbBr3 QDs hybrid film and (b) 062T SIBS/p-QDs hybrid film with a molar ratio of 1 : 1

4.4 Morphology Study of SIBS/p-QDs Hybrid Films

The phase behavior of BCP is determined by two critical factors: χN, which is a product of the Flory-Hoggins parameter (χ) and the degree of polymerization (N) of the blocks, and the fraction of the total volume occupied by one of the blocks (*f*). The degree of the segregation between the two blocks is typically influenced by the temperature and the chemical composition of the blocks,[86] with χ representing the level of segregation. BCP tends to assume one of the seven specific ordered phases, primarily determined by the relative lengths of the two constituent blocks.[28]

The morphology and phase behavior have been studied in our previous work.[87] The AFM phase images obtained in this study reveal the microphase-separated morphology of

SIBS films and SIBS/p-QDs hybrid films. The hexagonally packed cylindrical microphase separation structure between the PS and PIB blocks of SIBS is evident in the images, with bright and dark domains representing the PS and PIB domains, respectively. The contrast in the material properties between these domains is visible in the phase image, indicating a typical example of microphase separation in block copolymers. The control samples, consisting of 073T SIBS (Figure 20a, b) and 062T SIBS films (Figure 21a, b), exhibit a consistent microphase separation structure, with the difference being observed in their cylinder orientations. The 073T film shows vertical alignment, while the 062T SIBS film displays a tilted orientation. The bright domains are associated with the stiffer material, indicating that the interaction between the tip and the sample is dominated by repulsive forces.[87]

Interestingly, the SIBS/p-QDs hybrid film with a molar ratio of 5 : 2 (Figures 20d and 21d) displays an unaltered microphase structure. This observation suggests that the addition of a moderate amount of p-QDs to the SIBS matrix does not significantly affect the balance between the interfacial energy and the entropic loss associated with the microphase separation.[88] The lack of significant morphology changes in the hybrid film may be attributed to the similar chemical composition and interaction parameters between the PIB chains in SIBS and the p-QDs may promote their homogenous distribution within the matrix, thus avoiding any drastic changes in the morphology. However, hybrid films with a relatively high content of p-QDs, as depicted in Figures 20f and 21f, show no observable microphase separation structure, suggesting that the p-QDs interact with the block copolymer. The significant impact of p-QDs on the morphology of the hybrid film is evident from the disrupted cylindrical microphase separation structure, indicating a strong interaction between p-QDs and SIBS. The non-uniform of p-QDs in the hybrid film leads to their aggregation in clusters due to the dominant attractive forces of the p-QDs. This aggregation, coupled with the high presence of p-QDs, can significantly alter the morphology of the microphase-separated structure of SIBS. Specifically, the interfacial energy decrease, leading to a disruption of the microphase separation morphology. Additionally, the disruption of the p-QDs throughout a given domain, including at the PS/PIB boundaries, reduces the number of unfavorable PS/PIB contacts, ultimately decreasing the interfacial tension between the phases.[48,89–91] These results highlight the importance of understanding the intricate interplay between the chemical composition and morphology of BCPs and their interaction with p-QDs, which can have a significant effect on their microphase behavior.

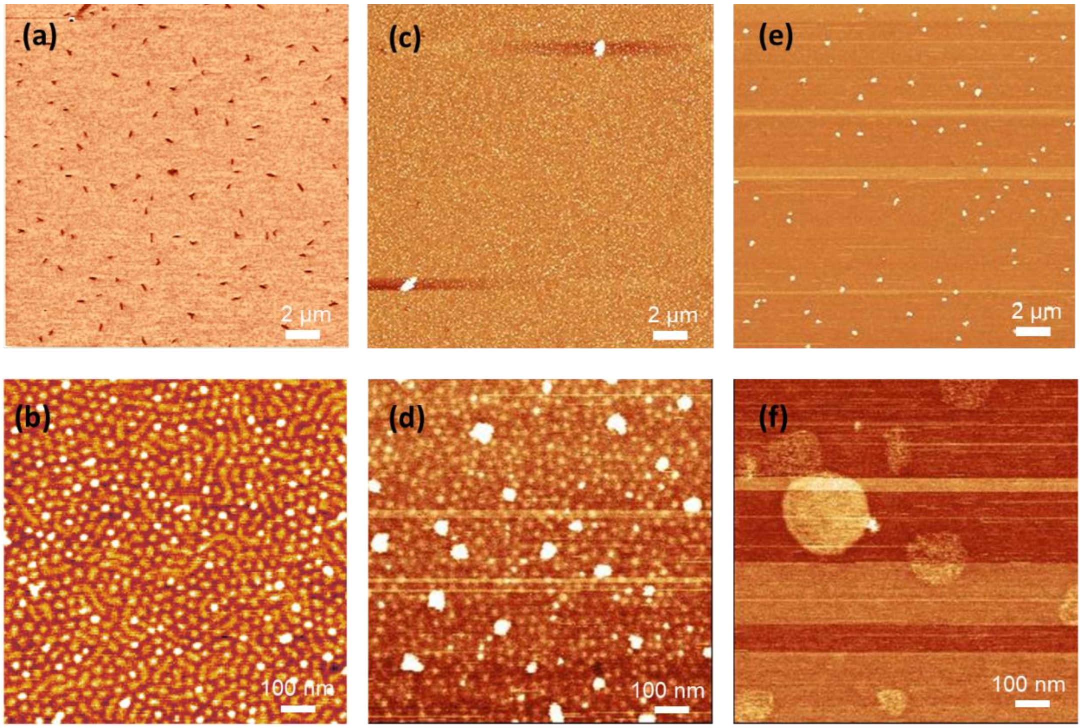

Figure 20. AFM phase images of (a) pure 073T SIBS film and (b) its higher magnification. (c) 073T SIBS/p-QDs hybrid film with a molar ratio of 5 : 2 and (d) its magnification. (e) 073T SIBS/p-QDs hybrid film with a molar ratio of 1 : 1 and (f) its magnification.

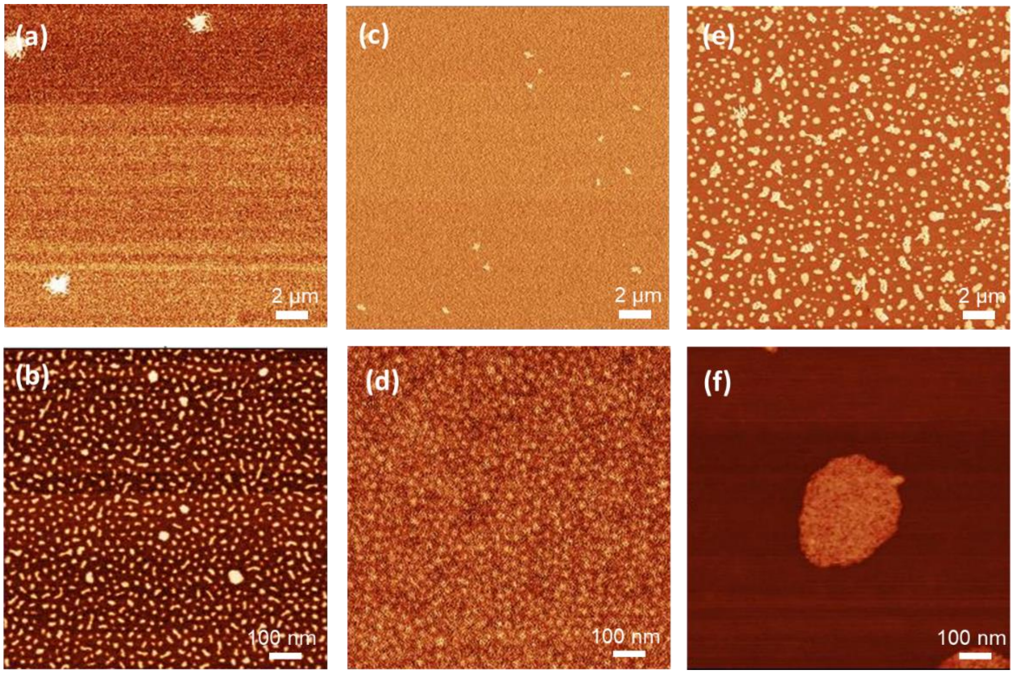

Figure 21. AFM phase images of (a) pure 062T SIBS film and (b) its higher magnification. (c) 062T SIBS/p-QDs hybrid film with a molar ratio of 5 : 2 and (d) its magnification. (e) 062T SIBS/p-QDs hybrid film with a molar ratio of 1 : 1 and (f) its magnification.

CHAPTER V. CONCLUSION AND FUTURE WORKS

This study provides a promising approach for synthesizing functional polymeric ligands for MHP QDs, and integrating the p-QDs with a block copolymer TPE matrix for the creation of flexible and stretchable optical materials. The p-QDs exhibit a slight blue shift in their absorption and emission peaks, which can be attributed to their reduced nanocrystal size and decreased trap states. When incorporated into copolymer matrix such as SIBS, the p-QDs with polymeric ligands show a strong affinity for the polymer matrix, resulting in a more stable hybrid film compared to SIBS/QDs films.

Furthermore, the morphology of the SIBS/p-QDs hybrid films reveals that the at high loadings of p-QDs, they cansubstantially alter the microphase separated morphology of the copolymer matrix. The p-QDs are also expected to be aligned with the PIB block due to the strong affinity with the polymer ligand.These findings suggest the potential for creating stable, stretchable, hybrid optical materials with nanometer size control of the internal structure.

While the current work focuses on synthesizing and designing polymeric ligands and conducting stability tests for p-QDs and SIBS/p-QDs hybrid films, more systematic study is needed for these hybrid materials. For instance, XRD and X-ray scattering can provide insights into the crystalline structure of p-QDs as well as their spatial alignment in the soft matrix. Additionally, DSC and TGA analysis can help elucidate the phase transitionsand thermal stabilities of the hybrid materials.

REFERENCES

(1) Zhang, W.; Eperon, G. E.; Snaith, H. J. Metal Halide Perovskites for Energy Applications. *Nat. Energy* **2016**, *1* (6). https://doi.org/10.1038/nenergy.2016.48.

(2) Kang, J.; Cho, J. H. Organic-Inorganic Hybrid Perovskite Electronics. *Phys. Chem. Chem. Phys.* **2020**, *22* (24), 13347–13357. https://doi.org/10.1039/d0cp01843k.

(3) Parobek, D.; Dong, Y.; Qiao, T.; Son, D. H. Direct Hot-Injection Synthesis of Mn-Doped CsPbBr3 Nanocrystals. *Chem. Mater.* **2018**, *30* (9), 2939–2944. https://doi.org/10.1021/acs.chemmater.8b00310.

(4) Dong, Y.; Qiao, T.; Kim, D.; Parobek, D.; Rossi, D.; Son, D. H. Precise Control of Quantum Confinement in Cesium Lead Halide Perovskite Quantum Dots via Thermodynamic Equilibrium. *Nano Lett.* **2018**, *18* (6), 3716–3722. https://doi.org/10.1021/acs.nanolett.8b00861.

(5) Li, Y.; Zhang, X.; Huang, H.; Kershaw, S. V.; Rogach, A. L. Advances in Metal Halide Perovskite Nanocrystals: Synthetic Strategies, Growth Mechanisms, and Optoelectronic Applications. *Mater. Today* **2020**, *32* (February), 204–221. https://doi.org/10.1016/j.mattod.2019.06.007.

(6) Stoumpos, C. C.; Kanatzidis, M. G. Halide Perovskites: Poor Man's High-Performance Semiconductors. *Adv. Mater.* **2016**, *28* (28), 5778–5793. https://doi.org/10.1002/adma.201600265.

(7) Protesescu, L.; Yakunin, S.; Bodnarchuk, M. I.; Krieg, F.; Caputo, R.; Hendon, C. H.; Yang, R. X.; Walsh, A.; Kovalenko, M. V. Nanocrystals of Cesium Lead Halide Perovskites (CsPbX3, X = Cl, Br, and I): Novel Optoelectronic Materials Showing Bright Emission with Wide Color Gamut. *Nano Lett.* **2015**, *15* (6), 3692–3696. https://doi.org/10.1021/nl5048779.

(8) Ercan, E.; Tsai, P. C.; Chen, J. Y.; Lam, J. Y.; Hsu, L. C.; Chueh, C. C.; Chen, W. C. Stretchable and Ambient Stable Perovskite/Polymer Luminous Hybrid Nanofibers of Multicolor Fiber Mats and Their White LED Applications. *ACS Appl. Mater. Interfaces* **2019**, *11* (26), 23605–23615. https://doi.org/10.1021/acsami.9b05527.

(9) Aharon, S.; Etgar, L. Two Dimensional Organometal Halide Perovskite Nanorods with Tunable Optical Properties. *Nano Lett.* **2016**, *16* (5), 3230–3235. https://doi.org/10.1021/acs.nanolett.6b00665.

(10) Ha, S. T.; Su, R.; Xing, J.; Zhang, Q.; Xiong, Q. Metal Halide Perovskite Nanomaterials: Synthesis and Applications. *Chem. Sci.* **2017**, *8* (4), 2522–2536. https://doi.org/10.1039/c6sc04474c.

(11) Xing, J.; Yan, F.; Zhao, Y.; Chen, S.; Yu, H.; Zhang, Q.; Zeng, R.; Demir, H. V.; Sun, X.; Huan, A.; Xiong, Q. High-Efficiency Light-Emitting Diodes of Organometal Halide Perovskite Amorphous Nanoparticles. *ACS Nano* **2016**, *10* (7), 6623–6630. https://doi.org/10.1021/acsnano.6b01540.

(12) Zhao, Y.; Li, J.; Dong, Y.; Song, J. Synthesis of Colloidal Halide Perovskite Quantum Dots/Nanocrystals: Progresses and Advances. *Isr. J. Chem.* **2019**, *59* (8), 649–660. https://doi.org/10.1002/ijch.201900009.

(13) King, G.; Woodward, P. M. Cation Ordering in Perovskites. *J. Mater. Chem.* **2010**, *20* (28), 5785–5796. https://doi.org/10.1039/b926757c.

(14) Wang, D.; Wright, M.; Elumalai, N. K.; Uddin, A. Stability of Perovskite Solar Cells. *Sol. Energy Mater. Sol. Cells* **2016**, *147*, 255–275. https://doi.org/10.1016/j.solmat.2015.12.025.

(15) Zhang, H.; Ren, X.; Chen, X.; Mao, J.; Cheng, J.; Zhao, Y.; Liu, Y.; Milic, J.; Yin, W. J.; Grätzel, M.; Choy, W. C. H. Improving the Stability and Performance of Perovskite Solar Cells: Via off-the-Shelf Post-Device Ligand Treatment. *Energy Environ. Sci.* **2018**, *11* (8), 2253–2262. https://doi.org/10.1039/c8ee00580j.

(16) A.S. Bhalla; Guo, R.; Roy, R. The Perovskite Structure – a Review of Its Role in Ceramic Science and Technology. *Mater. Res. Innov.* **2000**, 3–26.

(17) Liu, Y.; Chen, T.; Jin, Z.; Li, M.; Zhang, D.; Duan, L.; Zhao, Z.; Wang, C. Tough,

Stable and Self-Healing Luminescent Perovskite-Polymer Matrix Applicable to All Harsh Aquatic Environments. *Nat. Commun.* **2022**, *13* (1), 1–11. https://doi.org/10.1038/s41467-022-29084-z.

(18) Jeong, M.; Choi, I. W.; Go, E. M.; Cho, Y.; Kim, M.; Lee, B.; Jeong, S.; Jo, Y.; Choi, H. W.; Lee, J.; Bae, J. H.; Kwak, S. K.; Kim, D. S.; Yang, C. Stable Perovskite Solar Cells with Efficiency Exceeding 24.8% and 0.3-V Voltage Loss. *Science (80-.).* **2020**, *369* (6511), 1615–1620. https://doi.org/10.1126/science.abb7167.

(19) Xiang, W.; Liu, S.; Tress, W. A Review on the Stability of Inorganic Metal Halide Perovskites: Challenges and Opportunities for Stable Solar Cells. *Energy Environ. Sci.* **2021**, *14* (4), 2090–2113. https://doi.org/10.1039/d1ee00157d.

(20) Li, M.; Li, H.; Fu, J.; Liang, T.; Ma, W. Recent Progress on the Stability of Perovskite Solar Cells in a Humid Environment. *J. Phys. Chem. C* **2020**, *124* (50), 27251–27266. https://doi.org/10.1021/acs.jpcc.0c08019.

(21) Jeong, B.; Han, H.; Park, C. Micro- and Nanopatterning of Halide Perovskites Where Crystal Engineering for Emerging Photoelectronics Meets Integrated Device Array Technology. *Adv. Mater.* **2020**, *32* (30), 1–35. https://doi.org/10.1002/adma.202000597.

(22) Mao, J.; Sha, W. E. I.; Zhang, H.; Ren, X.; Zhuang, J.; Roy, V. A. L.; Wong, K. S.;

Choy, W. C. H. Novel Direct Nanopatterning Approach to Fabricate Periodically Nanostructured Perovskite for Optoelectronic Applications. *Adv. Funct. Mater.* **2017**, *27* (10), 1–10. https://doi.org/10.1002/adfm.201606525.

(23) Gholipour, B.; Adamo, G.; Cortecchia, D.; Krishnamoorthy, H. N. S.; Birowosuto, M. D.; Zheludev, N. I.; Soci, C. Organometallic Perovskite Metasurfaces. *Adv. Mater.* **2017**, *29* (9), 1–6. https://doi.org/10.1002/adma.201604268.

(24) Wang, Z.; Yang, T.; Zhang, Y.; Ou, Q.; Lin, H.; Zhang, Q.; Chen, H.; Hoh, H. Y.; Jia, B.; Bao, Q. Flat Lenses Based on 2D Perovskite Nanosheets. *Adv. Mater.* **2020**, *32* (30), 1–9. https://doi.org/10.1002/adma.202001388.

(25) Annable, T.; Ettelaie, R.; Ettelaie, R. Thermodynamics of Phase Separation in Mixtures of Associating Polymers and Homopolymers in Solution. *Macromolecules* **1994**, *27* (20), 5616–5622. https://doi.org/10.1021/ma00098a015.

(26) Wang, X.; Goswami, M.; Kumar, R.; Sumpter, B. G.; Mays, J. Morphologies of Block Copolymers Composed of Charged and Neutral Blocks. *Soft Matter* **2012**, *8* (11), 3036–3052. https://doi.org/10.1039/c2sm07223h.

(27) Fredrickson, G. H.; Bates, F. S. Dynamics of Block Copolymers: Theory and Experiment. *Annu. Rev. Mater. Sci.* **1996**, *26* (1), 501–550. https://doi.org/10.1146/annurev.ms.26.080196.002441.

(28) Schmia, K. S.; Eden, D.; Pecora, R.; Eden, D.; Garner, M. M.; Solutiotlc, M.;

Urbach, W.; Rondelez, F.; Hearst, J. E.; Klein, M. P.; Lopezmartinez, C.; Pastor, R. W.; Pecora, R.; Eden, D.; Pecora, R.; Allison, S. A.; Eden, D.; Pecora, R.; Pecora, R.; Bott, S. E.; Hagerman, P. J.; Yoshizaki, T.; Zimm, R. H.; Fujii, M.; Sorlie, S. S.; Pecora, R.; Roiunan, D. R.; Pecora, R.; Pecora, R.; Aragon, S. R.; Zimm, B. H.; Lerman, L. S.; Baldwin, R. L.; Renbasat, J. A.; Rloonifield, V. A.; Rloomfield, V. A.; Pecora, R.; Rill, R. L. Polymer-Polymer Phase Behavior. **1990**, *25* (1986).

(29) Kim, S. H.; Misner, M. J.; Xu, T.; Kimura, M.; Russell, T. P. Highly Oriented and Ordered Arrays from Block Copolymers via Solvent Evaporation. *Adv. Mater.* **2004**, *16* (3), 226–231. https://doi.org/10.1002/adma.200304906.

(30) Nicolas, J.; Ruzette, A. V.; Farcet, C.; Gérard, P.; Magnet, S.; Charleux, B. Nanostructured Latex Particles Synthesized by Nitroxide-Mediated Controlled/Living Free-Radical Polymerization in Emulsion. *Polymer (Guildf).* **2007**, *48* (24), 7029–7040. https://doi.org/10.1016/j.polymer.2007.09.039.

(31) Cui, H.; Chen, Z.; Zhong, S.; Wooley, K. L.; Pochan, D. J. Block Copolymer Assembly via Kinetic Control. *Science (80-.).* **2007**, *317* (5838), 647–650. https://doi.org/10.1126/science.1141768.

(32) Warren, S. C.; Messina, L. C.; Slaughter, L. S.; Kamperman, M.; Zhou, Q.; Gruner, S. M.; DiSalvo, F. J.; Wiesner, U. Ordered Mesoporous Materials from Metal Nanoparticle-Block Copolymer Self-Assembly. *Science (80-.).* **2008**, *320*

(5884), 1748–1752. https://doi.org/10.1126/science.1159950.

(33) Matyjaszewski, K.; Tsarevsky, N. V. Nanostructured Functional Materials Prepared by Atom Transfer Radical Polymerization. *Nat. Chem.* **2009**, *1* (4), 276–288. https://doi.org/10.1038/nchem.257.

(34) Bates, F. S.; Fredrickson, G. H. Block Copolymers-Designer Soft Materials. *Phys. Today* **1999**, *52* (2), 32–38. https://doi.org/10.1063/1.882522.

(35) Owen, J. S.; Park, J.; Trudeau, P. E.; Alivisatos, A. P. Reaction Chemistry and Ligand Exchange at Cadmium-Selenide Nanocrystal Surfaces. *J. Am. Chem. Soc.* **2008**, *130* (37), 12279–12281. https://doi.org/10.1021/ja804414f.

(36) Hong, R.; Fischer, N. O.; Emrick, T.; Rotello, V. M. Surface PEGylation and Ligand Exchange Chemistry of FePt Nanoparticles for Biological Applications. *Chem. Mater.* **2005**, *17* (18), 4617–4621. https://doi.org/10.1021/cm0507819.

(37) Allen C. Templeton, W. Peter Wuelfing, and R. W. M. Monolayer-Protected Cluster Molecules. *Acc. Chem. Res.* **2000**, *33* (1), 27–36.

(38) ELIZABETH GLOGOWSKI, RAVISUBHASH TANGIRALA, THOMAS P. RUSSELL, T. E.; Holdcroft, S.; Hay, A. S. Functionalization of Nanoparticles for Dispersion in Polymers and Assembly in Fluids. *J. Polym. Sci. Part A Polym. Chem.* **2006**, *44*, 5076–5086. https://doi.org/10.1002/pola.

(39) Kao, J.; Thorkelsson, K.; Bai, P.; Rancatore, B. J.; Xu, T. Toward Functional

Nanocomposites: Taking the Best of Nanoparticles, Polymers, and Small Molecules. *Chem. Soc. Rev.* **2013**, *42* (7), 2654–2678. https://doi.org/10.1039/c2cs35375j.

(40) Bockstaller, M. R.; Mickiewicz, R. A.; Thomas, E. L. Block Copolymer Nanocomposites: Perspectives for Tailored Functional Materials. *Adv. Mater.* **2005**, *17* (11), 1331–1349. https://doi.org/10.1002/adma.200500167.

(41) Tsutsumi, K.; Funaki, Y.; Hirokawa, Y.; Hashimoto, T. Selective Incorporation of Palladium Nanoparticles into Microphase-Separated Domains of Poly(2-Vinylpyridine)-Block-Polyisoprene. *Langmuir* **1999**, *15* (16), 5200–5203. https://doi.org/10.1021/la990246l.

(42) Huh, J.; Ginzburg, V. V.; Balazs, A. C. Thermodynamic Behavior of Particle/Diblock Copolymer Mixtures: Simulation and Theory. *Macromolecules* **2000**, *33* (21), 8085–8096. https://doi.org/10.1021/ma000708y.

(43) Chiu, J. J.; Kim, B. J.; Kramer, E. J.; Pine, D. J. Control of Nanoparticle Location in Block Copolymers. *J. Am. Chem. Soc.* **2005**, *127* (14), 5036–5037. https://doi.org/10.1021/ja050376i.

(44) Mackay, M. E.; Tuteja, A.; Duxbury, P. M.; Hawker, C. J.; Van Horn, B.; Guan, Z.; Chen, G.; Krishnan, R. S. General Strategies for Nanoparticle Dispersion. *Science (80-.).* **2006**, *311* (5768), 1740–1743.

https://doi.org/10.1126/science.1122225.

(45) Lauter-Pasyuk, V.; Lauter, H. J.; Ausserre, D.; Gallot, Y.; Cabuil, V.; Kornilov, E. I.; Hamdoun, B. Effect of Nanoparticle Size on the Internal Structure of Copolymer-Nanoparticles Composite Thin Films Studied by Neutron Reflection. *Phys. B Condens. Matter* **1997**, *241–243*, 1092–1094. https://doi.org/10.1016/S0921-4526(97)00877-6.

(46) Lee, J. Y.; Thompson, R. B.; Jasnow, D.; Balazs, A. C. Entropically Driven Formation of Hierarchically Ordered Nanocomposites. *Phys. Rev. Lett.* **2002**, *89* (15), 1–4. https://doi.org/10.1103/PhysRevLett.89.155503.

(47) Spontak, R. J.; Shankar, R.; Bowman, M. K.; Krishnan, A. S.; Hamersky, M. W.; Samseth, J.; Bockstaller, M. R.; Rasmussen, K. Selectivity- and Size-Induced Segregation of Molecular and Nanoscale Species in Microphase-Ordered Triblock Copolymers. *Nano Lett.* **2006**, *6* (9), 2115–2120. https://doi.org/10.1021/nl061205u.

(48) Matsen, M. W.; Thompson, R. B. Particle Distributions in a Block Copolymer Nanocomposite. *Macromolecules* **2008**, *41* (5), 1853–1860. https://doi.org/10.1021/ma7024545.

(49) Kim, B. J.; Fredrickson, G. H.; Kramer, E. J. Effect of Polymer Ligand Molecular Weight on Polymer-Coated Nanoparticle Location in Block Copolymers.

Macromolecules **2008**, *41* (2), 436–447. https://doi.org/10.1021/ma701931z.

(50) Chiu, J. J.; Kim, B. J.; Yi, G. R.; Bang, J.; Kramer, E. J.; Pine, D. J. Distribution of Nanoparticles in Lamellar Domains of Block Copolymers. *Macromolecules* **2007**, *40* (9), 3361–3365. https://doi.org/10.1021/ma061503d.

(51) Bockstaller, M. R.; Lapetnikov, Y.; Margel, S.; Thomas, E. L. Size-Selective Organization of Enthalpic Compatibilized Nanocrystals in Ternary Block Copolymer/Particle Mixtures. *J. Am. Chem. Soc.* **2003**, *125* (18), 5276–5277. https://doi.org/10.1021/ja034523t.

(52) Kim, B. J.; Bang, J.; Hawker, C. J.; Kramer, E. J. Effect of Areal Chain Density on the Location of Polymer-Modified Gold Nanoparticles in a Block Copolymer Template. *Macromolecules* **2006**, *39* (12), 4108–4114. https://doi.org/10.1021/ma060308w.

(53) Kim, B. J.; Chiu, J. J.; Yi, G. R.; Pine, D. J.; Kramer, E. J. Nanoparticle-Induced Phase Transitions in Diblock-Copolymer Films. *Adv. Mater.* **2005**, *17* (21), 2618–2622. https://doi.org/10.1002/adma.200500502.

(54) Lin, Y.; Böker, A.; He, J.; Sill, K.; Xiang, H.; Abetz, C.; Li, X.; Wang, J.; Emrick, T.; Long, S.; Wang, Q.; Balazs, A.; Russell, T. P. Self-Directed Self-Assembly of Nanoparticle/Copolymer Mixtures. *Nature* **2005**, *434* (7029), 55–59. https://doi.org/10.1038/nature03310.

(55) Hou, S.; Guo, Y.; Tang, Y.; Quan, Q. Synthesis and Stabilization of Colloidal Perovskite Nanocrystals by Multidentate Polymer Micelles. *ACS Appl. Mater. Interfaces* **2017**, *9* (22), 18417–18422. https://doi.org/10.1021/acsami.7b03445.

(56) Song, D. P.; Li, C.; Li, W.; Watkins, J. J. Block Copolymer Nanocomposites with High Refractive Index Contrast for One-Step Photonics. *ACS Nano* **2016**, *10* (1), 1216–1223. https://doi.org/10.1021/acsnano.5b06525.

(57) Kwak, J.; Mishra, A. K.; Lee, J.; Lee, K. S.; Choi, C.; Maiti, S.; Kim, M.; Kim, J. K. Fabrication of Sub-3 Nm Feature Size Based on Block Copolymer Self-Assembly for Next-Generation Nanolithography. *Macromolecules* **2017**, *50* (17), 6813–6818. https://doi.org/10.1021/acs.macromol.7b00945.

(58) Jennings, J.; Beija, M.; Kennon, J. T.; Willcock, H.; O’Reilly, R. K.; Rimmer, S.; Howdle, S. M. Advantages of Block Copolymer Synthesis by RAFT-Controlled Dispersion Polymerization in Supercritical Carbon Dioxide. *Macromolecules* **2013**, *46* (17), 6843–6851. https://doi.org/10.1021/ma401051e.

(59) You, I.; Kong, M.; Jeong, U. Block Copolymer Elastomers for Stretchable Electronics. *Acc. Chem. Res.* **2019**, *52* (1), 63–72. https://doi.org/10.1021/acs.accounts.8b00488.

(60) Sugiyama, F.; Kleinschmidt, A. T.; Kayser, L. V.; Alkhadra, M. A.; Wan, J. M. H.; Chiang, A. S. C.; Rodriquez, D.; Root, S. E.; Savagatrup, S.; Lipomi, D. J.

Stretchable and Degradable Semiconducting Block Copolymers. *Macromolecules* **2018**, *51* (15), 5944–5949. https://doi.org/10.1021/acs.macromol.8b00846.

(61) Hsu, L. C.; Isono, T.; Lin, Y. C.; Kobayashi, S.; Chiang, Y. C.; Jiang, D. H.; Hung, C. C.; Ercan, E.; Yang, W. C.; Hsieh, H. C.; Tajima, K.; Satoh, T.; Chen, W. C. Stretchable OFET Memories: Tuning the Morphology and the Charge-Trapping Ability of Conjugated Block Copolymers through Soft Segment Branching. *ACS Appl. Mater. Interfaces* **2021**, *13* (2), 2932–2943. https://doi.org/10.1021/acsami.0c18820.

(62) Hung, C. C.; Nakahira, S.; Chiu, Y. C.; Isono, T.; Wu, H. C.; Watanabe, K.; Chiang, Y. C.; Takashima, S.; Borsali, R.; Tung, S. H.; Satoh, T.; Chen, W. C. Control over Molecular Architectures of Carbohydrate-Based Block Copolymers for Stretchable Electrical Memory Devices. *Macromolecules* **2018**, *51* (13), 4966–4975. https://doi.org/10.1021/acs.macromol.8b00874.

(63) Kayser, L. V.; Russell, M. D.; Rodriquez, D.; Abuhamdieh, S. N.; Dhong, C.; Khan, S.; Stein, A. N.; Ramírez, J.; Lipomi, D. J. RAFT Polymerization of an Intrinsically Stretchable Water-Soluble Block Copolymer Scaffold for PEDOT. *Chem. Mater.* **2018**, *30* (13), 4459–4468. https://doi.org/10.1021/acs.chemmater.8b02040.

(64) Antony, P.; Puskas, J. E.; Kontopoulou, M. Investigation of the Rheological and Mechanical Properties of a Polystyrene-Polyisobutylene-Polystyrene Triblock

Copolymer and Its Blends With Polystyrene. *Polym. Eng. Sci.* **2003**, *43* (1), 243–253. https://doi.org/10.1002/pen.10021.

(65) Song, D. P.; Li, C.; Colella, N. S.; Lu, X.; Lee, J. H.; Watkins, J. J. Thermally Tunable Metallodielectric Photonic Crystals from the Self-Assembly of Brush Block Copolymers and Gold Nanoparticles. *Adv. Opt. Mater.* **2015**, *3* (9), 1169–1175. https://doi.org/10.1002/adom.201500116.

(66) Park, C.; Yoon, J.; Thomas, E. L. Enabling Nanotechnology with Self Assembled Block Copolymer Patterns. *Polymer (Guildf).* **2003**, *44* (22), 6725–6760. https://doi.org/10.1016/j.polymer.2003.08.011.

(67) Haryono, A.; Binder, W. H. Controlled Arrangement of Nanoparticle Arrays in Block-Copolymer Domains. *Small* **2006**, *2* (5), 600–611. https://doi.org/10.1002/smll.200500474.

(68) Cheng, J. Y.; Ross, C. A.; Smith, H. I.; Thomas, E. L. Templated Self-Assembly of Block Copolymers: Top-down Helps Bottom-Up. *Adv. Mater.* **2006**, *18* (19), 2505–2521. https://doi.org/10.1002/adma.200502651.

(69) Ranade, S. V.; Richard, R. E.; Helmus, M. N. Styrenic Block Copolymers for Biomaterial and Drug Delivery Applications. *Acta Biomater.* **2005**, *1* (1), 137–144. https://doi.org/10.1016/j.actbio.2004.09.004.

(70) Puskas, J. E.; Kaszas, G. Polyisobutylene-Based Thermoplastic Elastomers: A

Review. *Rubber Chemistry and Technology*. 1996, pp 462–475. https://doi.org/10.5254/1.3538381.

(71) Puskas, J. E.; Kwon, Y.; Altstädt, V.; Kontopoulou, M. Blends of Poly(2,6-Dimethyl-1,4-Phenylene Oxide) (PPO) with Polystyrene-Based Thermoplastic Rubbers: A Comparative Study. *Polymer (Guildf)*. **2007**, *48* (2), 590–597. https://doi.org/10.1016/j.polymer.2006.11.045.

(72) Pinchuk, L.; Wilson, G. J.; Barry, J. J.; Schoephoerster, R. T.; Parel, J. M.; Kennedy, J. P. Medical Applications of Poly(Styrene-Block-Isobutylene-Block-Styrene) ("SIBS"). *Biomaterials* **2008**, *29* (4), 448–460. https://doi.org/10.1016/j.biomaterials.2007.09.041.

(73) Gong, W.; Qi, R. Graft Copolymerization of Maleic Anhydride onto Low-Molecular-Weight Polyisobutylene Through Solvothermal Method. *J. Appl. Polym. Sci.* **2009**, *116* (5), 2658–2667. https://doi.org/10.1002/app.

(74) Kim, G.; Yoo, C. E.; Kim, M.; Kang, H. J.; Park, D.; Lee, M.; Huh, N. Noble Polymeric Surface Conjugated with Zwitterionic Moieties and Antibodies for the Isolation of Exosomes from Human Serum. *Bioconjug. Chem.* **2012**, *23* (10), 2114–2120. https://doi.org/10.1021/bc300339b.

(75) Wang, W.; Ji, X.; Kapur, A.; Zhang, C.; Mattoussi, H. A Multifunctional Polymer Combining the Imidazole and Zwitterion Motifs as a Biocompatible Compact

Coating for Quantum Dots. *J. Am. Chem. Soc.* **2015**, *137* (44), 14158–14172. https://doi.org/10.1021/jacs.5b08915.

(76) Nakason, C.; Kaesaman, A.; Supasanthitikul, P. The Grafting of Maleic Anhydride onto Natural Rubber. *Polym. Test.* **2004**, *23* (1), 35–41. https://doi.org/10.1016/S0142-9418(03)00059-X.

(77) Yanhan Shen, Rongrong Qi, Qiaochu Liu, C. Z. Solvothermal Preparation and Characterization of Maleic Anhydride Grafting High Density Polyethylene Copolymer. *J. Appl. Polym. Sci.* **2007**, *104* (5), 3443–3452. https://doi.org/10.1002/app.

(78) Sclavons, M.; Franquinet, P.; Carlier, V.; Verfaillie, G.; Fallais, I.; Legras, R.; Laurent, M.; Thyrion, F. C. Quantification of the Maleic Anhydride Grafted onto Polypropylene by Chemical and Viscosimetric Titrations, and FTIR Spectroscopy. *Polymer (Guildf).* **2000**, *41* (6), 1989–1999. https://doi.org/10.1016/S0032-3861(99)00377-8.

(79) Raja, S. N.; Bekenstein, Y.; Koc, M. A.; Fischer, S.; Zhang, D.; Lin, L.; Ritchie, R. O.; Yang, P.; Alivisatos, A. P. Encapsulation of Perovskite Nanocrystals into Macroscale Polymer Matrices: Enhanced Stability and Polarization. *ACS Appl. Mater. Interfaces* **2016**, *8* (51), 35523–35533. https://doi.org/10.1021/acsami.6b09443.

(80) Van Sark, W. G. J. H. M.; Frederix, P. L. T. M.; Van den Heuvel, D. J.; Gerritsen, H. C.; Bol, A. A.; Van Lingen, J. N. J.; De Mello Donegá, C.; Meijerink, A. Photooxidation and Photobleaching of Single CdSe/ZnS Quantum Dots Probed by Room-Temperature Time-Resolved Spectroscopy. *J. Phys. Chem. B* **2001**, *105* (35), 8281–8284. https://doi.org/10.1021/jp012018h.

(81) Park, Y. S.; Guo, S.; Makarov, N. S.; Klimov, V. I. Room Temperature Single-Photon Emission from Individual Perovskite Quantum Dots. *ACS Nano* **2015**, *9* (10), 10386–10393. https://doi.org/10.1021/acsnano.5b04584.

(82) Maes, J.; Balcaen, L.; Drijvers, E.; Zhao, Q.; De Roo, J.; Vantomme, A.; Vanhaecke, F.; Geiregat, P.; Hens, Z. Light Absorption Coefficient of CsPbBr3 Perovskite Nanocrystals. *J. Phys. Chem. Lett.* **2018**, *9* (11), 3093–3097. https://doi.org/10.1021/acs.jpclett.8b01065.

(83) Yuan, G.; Ritchie, C.; Ritter, M.; Murphy, S.; Gómez, D. E.; Mulvaney, P. The Degradation and Blinking of Single CsPbI3 Perovskite Quantum Dots. *J. Phys. Chem. C* **2018**, *122* (25), 13407–13415. https://doi.org/10.1021/acs.jpcc.7b11168.

(84) Seth, S.; Mondal, N.; Patra, S.; Samanta, A. Fluorescence Blinking and Photoactivation of All-Inorganic Perovskite Nanocrystals CsPbBr3 and CsPbBr2I. *J. Phys. Chem. Lett.* **2016**, *7* (2), 266–271. https://doi.org/10.1021/acs.jpclett.5b02639.

(85) Eperon, G. E.; Habisreutinger, S. N.; Leijtens, T.; Bruijnaers, B. J.; Van Franeker, J. J.; Dequilettes, D. W.; Pathak, S.; Sutton, R. J.; Grancini, G.; Ginger, D. S.; Janssen, R. A. J.; Petrozza, A.; Snaith, H. J. The Importance of Moisture in Hybrid Lead Halide Perovskite Thin Film Fabrication. *ACS Nano* **2015**, *9* (9), 9380–9393. https://doi.org/10.1021/acsnano.5b03626.

(86) Rubatat, L.; Shi, Z.; Diat, O.; Holdcroft, S.; Frisken, B. J. Structural Study of Proton-Conducting Fluorous Block Copolymer Membranes. *Macromolecules* **2006**, *39* (2), 720–730. https://doi.org/10.1021/ma0520139.

(87) Shen, N.; Liu, S.; Kasbe, P.; Khabaz, F.; Kennedy, J. P.; Xu, W. Macromolecular Engineering and Additive Manufacturing of Poly(Styrene - b - Isobutylene - b - Styrene). **2021**. https://doi.org/10.1021/acsapm.1c00616.

(88) Khanna, V.; Cochran, E. W.; Hexemer, A.; Stein, G. E.; Fredrickson, G. H.; Kramer, E. J.; Li, X.; Wang, J.; Hahn, S. F. Effect of Chain Architecture and Surface Energies on the Ordering Behavior of Lamellar and Cylinder Forming Block Copolymers. *Macromolecules* **2006**, *39* (26), 9346–9356. https://doi.org/10.1021/ma0609228.

(89) Yeh, S. W.; Wei, K. H.; Sun, Y. Sen; Jeng, U. S.; Liang, K. S. CdS Nanoparticles Induce a Morphological Transformation of Poly(Styrene-b-4-Vinylpyridine) from Hexagonally Packed Cylinders to a Lamellar Structure. *Macromolecules* **2005**, *38* (15), 6559–6565. https://doi.org/10.1021/ma047653a.

(90) Kim, J.; Green, P. F. Directed Assembly of Nanoparticles in Block Copolymer Thin Films: Role of Defects. *Macromolecules* **2010**, *43* (24), 10452–10456. https://doi.org/10.1021/ma101883w.

(91) Listak, J.; Hakem, I. F.; Ryu, H. J.; Rangou, S.; Politakos, N.; Misichronis, K.; Avgeropoulos, A.; Bockstaller, M. R. Effect of Chain Architecture on the Compatibility of Block Copolymer/Nanoparticle Blends. *Macromolecules* **2009**, *42* (15), 5766–5773. https://doi.org/10.1021/ma900600n.